

# Single Dielectric Barrier Discharge Plasma Actuator Modeling and Validation

**Benjamin E. Mertz and Thomas C. Corke**

University of Notre Dame, Institute for Flow Physics and Control, Aerospace and Mechanical Engineering Department, Notre Dame, IN 46556, USA

(Received January, 2010)

Single Dielectric Barrier Discharge (SDBD) plasma actuators have gained a great deal of world-wide interest for flow control applications. With this has come the need for flow-interaction models of plasma actuators that can be used in computational flow simulations. SDBD plasma actuators consist of two electrodes, one uncovered and exposed to the air and the other encapsulated by a dielectric material. An AC electric potential is supplied to the electrodes. When the AC potential is large enough, the air in the region over the encapsulated electrode ionizes. The ionized air in the presence of the electric field results in a space-time dependent body force vector field. The body force is the mechanism for flow control. This work describes a semi-empirical model that has been developed that captures the dynamic nature of the local air ionization and time-dependent body force vector distribution. Validation of the model includes comparisons to experimentally measured space-time charge distribution and the time-resolved and time-averaged body force. Two flow simulations are then used to further validate the SDBD plasma actuator model. These involved an impulsively started plasma actuator in still air, and the flow around a circular cylinder in which plasma actuators were used to suppress the Karman vortex street. In both cases, the simulations agreed well with the experiments.

**Key Words:** Plasma Actuator, Dielectric Barrier Discharge, Flow Control

---

## CONTENTS

<b>1. Introduction</b>	<b>1</b>
1.1. Objective	5
<b>2. SDBD Plasma Actuator Model</b>	<b>6</b>
2.1. Lumped-element Circuit Model	8
2.2. Body Force Model Results	10
2.3. Body Force Validation	12
<b>3. Flow Simulation Results</b>	<b>17</b>
3.1. Impulsively Started Flow	18
3.2. Cylinder Unsteady Wake Suppression	20
<b>4. Conclusions</b>	<b>22</b>

## 1. Introduction

Single-dielectric barrier discharge (SDBD) plasma actuators have been used effectively for flow control purposes in a variety of applications. These applications range from lift augmentation and boundary layer separation control, to jet mixing enhancement that

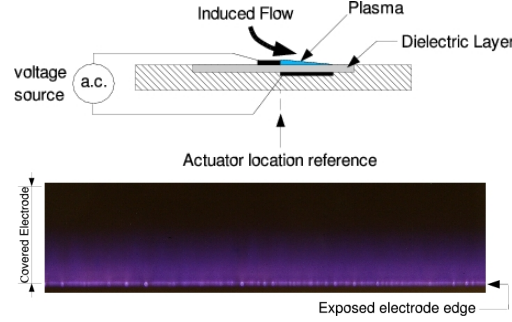


FIGURE 1. Schematic illustration of SDBD plasma actuator (top) and photograph of ionized air at 1 atm. pressure that forms over electrode covered by dielectric layer (bottom).

are among many others described in review articles (Corke *et al.* 2007, 2009). Some of the reasons for the popularity of these actuators is their simplicity, their high frequency response, low power consumption (2-40 Watts/ft of span (Post & Corke 2005)), and that they are fully electrical with no moving parts.

The predominant SDBD configuration used for flow control consists of two electrodes, one exposed to the air and the other encapsulated by a dielectric material. The electrodes are generally arranged asymmetrically. An example configuration is shown in the top part of Figure 1. The SDBD plasma actuator has the electrical properties of a capacitor and therefore it is powered by an AC voltage source. A large enough AC voltage causes the air over the encapsulated electrode to weakly ionize. The ionization fraction is typically less than 1 PPM. In the classic description, the ionized air is a “plasma,” which is why these are referred to as “plasma actuators”. The ionized air appears purple, which is a characteristic of the composition of the air as ionized components recombine and de-excite (Davidson & O’Neil 1964). The emission intensity is extremely low, requiring a darkened space to view by eye. A photograph of the ionized air produced by a plasma actuator is shown in the bottom part of Figure 1.

The ionized air, in the presence of the electric field produced by the arrangement of the electrodes, results in a body force vector field that acts on the ambient (non-ionized, neutrally charged) air. The body force is the mechanism for active aerodynamic control. In determining the response of the ambient air, the body force appears as a term on the right-hand-side of the fluid momentum equation.

For a single dielectric barrier discharge, during one-half of the AC cycle, electrons leave the metal electrode and move towards the dielectric where they accumulate locally. In the reverse half of the cycle, electrons are supplied by surface discharges on the dielectric and move toward the metal electrode. The time scale of the process depends on the gas composition, excitation frequency and other parameters. In air at atmospheric pressure, it occurs within a few tens of nanoseconds (Falkenstein & Coogan 1997). A one-dimensional model for the dielectric barrier discharge dynamics was developed by Massines and co-workers (Massines *et al.* 1998; Rabehi *et al.* October, 23-26, 1994, pp. 840-845; BenGadri *et al.* August, 23-26, 1994, pp. 228-229). It was based on the numerical solution of the electron and ion continuity and momentum transfer equations coupled to Poisson’s equation. As is typical in high pressure discharges, the electrons and ions were assumed to be in equilibrium with the electric field. Their model gave space and time variations in the electric field, and the electron and ion densities. The charge accumulation on the dielectric as the discharge develops was taken into account, and the voltage boundary

conditions for dielectrics were derived by considering an equivalent circuit of the gas gap in series with the equivalent capacitor of the dielectric.

Enloe *et al.* (2004a) studied the space-time evolution of the ionized air light-emission over a surface mounted SDBD plasma actuator using a photo-multiplier tube (PMT) fitted with a double-slit aperture to focus on a narrow 2-D region of the plasma. The slit was parallel to the edge of the exposed electrode and could be moved to different locations over the electrode covered by the dielectric. A sample time series from Orlov (2006) of the PMT output that was acquired phase-locked with the AC input to the actuator is shown in Figure 2. Also shown for reference is the AC input supplied to the electrodes. The light emission is taken as an indication of the plasma density, which is a good assumption based on the disparate time scales between the recombination time (order of  $10^{-8}$ sec)(Vidmar & Stalter 2003) versus the discharge time scale (order of  $10^{-3}$ sec).

There are several fundamental features of light emission time series. The first is that the air is ionized only over part of the AC cycle. When it does ionize, its character is different between the first and second halves of the AC cycle. This is the second fundamental feature. The final feature is that the light emission is made up of narrow spikes that might indicate numerous micro-discharges. Similar observations have been documented by Enloe *et al.* (2004a), Massines *et al.* (1998), and Eliasson & Kogelschatz (1991); Kogelschatz (1997), which generally characterize this process as a dielectric barrier discharge (DBD).

The explanation for the difference in the emission character in the two half-cycles is associated with the source of electrons. During the negative-going half cycle, the electrons originate from the bare electrode, which is essentially an infinite source that readily gives them up. In the positive-going half cycle, the electrons originate from the dielectric surface. These apparently do not come off as readily, or when they do, they come in the form of fewer, larger micro-discharges. This asymmetry has been modeled by Boeuf *et al.* (2007) and Orlov *et al.* (2008), and plays an important role in the efficiency of the momentum coupling to the neutrals. It further suggests some optimization can come in the selection of the AC waveform to improve the performance of the plasma actuator.

A composite of light emission time series like the one in Figure 2, but measured at different positions over the dielectric surface, is shown in Figure 3. These are shown as contours of constant light emission intensity for one period,  $T$ , of the AC cycle. The  $x$  axis is the distance over the covered electrode measured from the edge of the exposed electrode at the interface of the covered electrode.

The space-time character of the plasma light-emission over the covered electrode has a number of interesting features. For example, there is a sharp amplitude peak near the edge of the exposed electrode at the first initiation of the plasma. As time increases, the plasma sweeps out from the junction to cover a portion of the encapsulated electrode. This was similarly noted by Gibalov & Pietsch (2000). As the plasma sweeps out away from the edge of the exposed electrode, its light emission appears to become less intense. Estimates(Enloe *et al.* 2004a; Orlov 2006; Orlov *et al.* 2006) indicate that the intensity decreases exponentially from the junction. This led to the use of an exponential weighting for correcting the spatial dependence of the plasma actuator body force in earlier electrostatic flow simulations(Orlov *et al.* 2003; Orlov & Corke 2005; Voikov *et al.* 2004). Two of the global features of the space-time evolution of the plasma formation are the velocity at which the plasma front moves across the dielectric, and the maximum extent of the plasma during the AC cycle. The velocity is represented by the slope,  $dx/dt$ , of the front. In Figure 3, the velocity of the fronts is approximately the same for the two halves of the AC cycle, but the plasma extent differs. Orlov (2006) investigated the effects of voltage and AC frequency on the extent and propagation velocity of the discharge. He found that

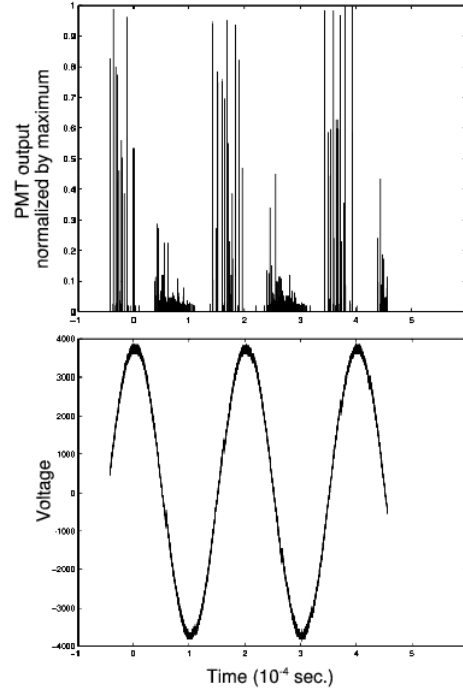


FIGURE 2. Time series of PMT output (top) that is viewing ionized air light emission at one location over electrode covered by dielectric, and corresponding AC input (bottom) to plasma actuator. (from Orlov(Orlov 2006))

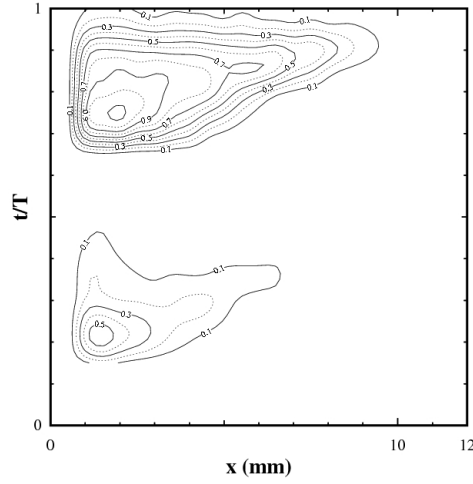


FIGURE 3. Space-time variation of the measured plasma light emission for SDBD plasma actuator corresponding to one period,  $T$ , of the input AC cycle. (from Orlov et al.(Orlov 2006; Orlov *et al.* 2006))

the maximum extent increased linearly with increasing AC voltage amplitude, and was independent of the AC frequency. However, the velocity of the plasma front increased linearly with both AC amplitude and frequency. In Orlov's measurements, the velocity of the discharge front ranged from 70 to 190 m/s.

Wall-mounted plasma actuators with an asymmetric electrode design like that shown

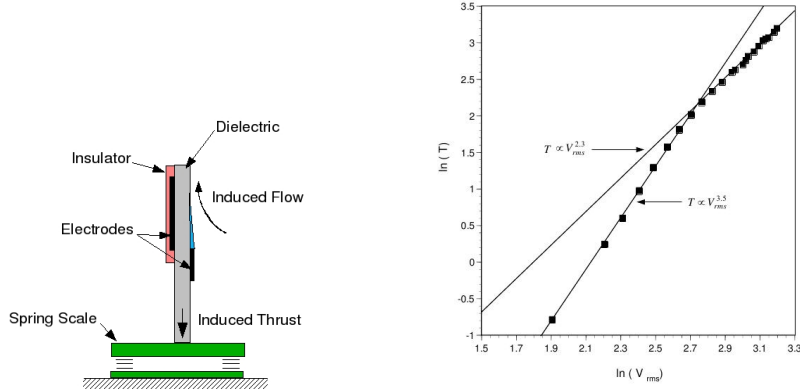


FIGURE 4. Schematic of experimental setup for measuring induced thrust from SDBD plasma actuator (left) and measured thrust versus applied AC voltage (right). (from Thomas *et al.* (2010))

in Figure 1, induce a velocity field similar to that of a tangential wall jet. Enloe *et al.* (2004b) correlated the reaction force (thrust) generated by the induced flow with the actuator AC amplitude. A similar experiment was performed by Thomas *et al.* (2010) to investigate parameters in the actuator design. A schematic of their setup and sample results are shown in Figure 4. At the lower voltages, the induced thrust was found to be proportional to  $V_{AC}^{3.5}$ . This was first observed by Enloe *et al.* (2004b). Thomas *et al.* (2010) verified consistency between the reaction force and the fluid momentum by integrating the velocity profiles downstream of the actuator. Post (2004) found that the maximum induced velocity was proportional to  $V_{AC}^{3.5}$ , which is consistent with conserved momentum in the self-similar velocity profile region near the actuator. At the highest voltages, the thrust change with voltage still appears to follow a power law relation, although the exponent is smaller and not necessarily universally accepted. The voltage at which the power-law exponent changes is a function of the area of the covered electrode, with a smaller area causing the change to occur at lower voltages. Most importantly, these experiments demonstrate that the thrust change with applied voltage is always greater than quadratic. The ability to duplicate this scaling behavior is one criterion by which numerical models for SDBD plasma actuators must be judged.

Attempts at modeling plasma actuators can be divided into two groups: first-principle charged-particle simulations, and empirical/semi-empirical models. Charged particle simulations require the self-consistent solution of complex chemistry and species transport equations, Poisson's equation, and the Navier-Stokes equations (Singh & Roy 2008). While this approach is able to accurately describe the different plasma discharge processes, it is extremely computationally intensive. As a result, it is often limited to a single "streamer", or a single discharge event. Over the AC time scale, the plasma is comprised of millions of streamers which makes it difficult to relate charged particle simulations to the bulk plasma actuator behavior.

Empirical and semi-empirical models attempt to capture the ionization effects of the plasma actuator without directly modeling the chemistry. Instead they focus on the bulk characteristics of the air and dielectric layer. One such approach by Orlov (2006); Orlov *et al.* (2006) modeled the actuator as a parallel arrangement of resistors, capacitors and diodes. This model was validated in terms of the plasma light emission characteristics over the AC period, like those in Figure 3.

### 1.1. Objective

The object of the present work was to further refine the Orlov approach to included a formulation in general curvilinear coordinates, and to remove a noted computational grid dependence. The model would then be validated with regard to both the time-averaged body force and time-resolved body force. The time-resolved body force validation would require a new experimental approach that would be based on relating the unsteady body force to the generated acoustics. Two flow simulations would then used to further validate the SDBD plasma actuator model. These would involve an impulsively started plasma actuator in still air, and the flow around a circular cylinder in which plasma actuators were used to suppress the Karman vortex street.

## 2. SDBD Plasma Actuator Model

The governing equations for the electrostatic plasma actuator model are presented in this section. The electrostatic formulation is based on the assumption that the plasma formation and fluid flow response can be decoupled due to the large disparities in the characteristic velocities associated with each process. For example, the characteristic velocities of the fluid transport under consideration range from 10 to 100 m/s, while for electron temperatures ranging between 1000 to 10000 K, the electron velocity, which is the characteristic velocity of the plasma, is of the order of  $10^5$  to  $10^6$  m/s (Vidmar & Stalter 2003).

This disparity in characteristic time scales suggests that the one can treat the AC plasma generation as a quasi-steady process in which the ions and electrons in the plasma are able to spatially redistribute themselves to offset the electric potential in a time scale that is much shorter than the AC period, and fluid response. As a result, the plasma actuator body force,  $f_B$  can be estimated through the Maxwell electrostatic body force equations as

$$\vec{f}_B = \rho \vec{E}, \quad (2.1)$$

where  $\rho$  is the charge density, and  $\vec{E}$  is the electric field. The electric field can be derived from the gradient of a scalar potential,  $\phi$ , namely

$$\vec{E} = -\nabla\phi. \quad (2.2)$$

From Gauss's law, the potential can be related to the charge density by,

$$\nabla \cdot (\epsilon_r \nabla \phi) = -\frac{\rho}{\epsilon_0}, \quad (2.3)$$

where  $\epsilon_0$  is the permittivity of free space and  $\epsilon_r$  is the relative permittivity of the medium.

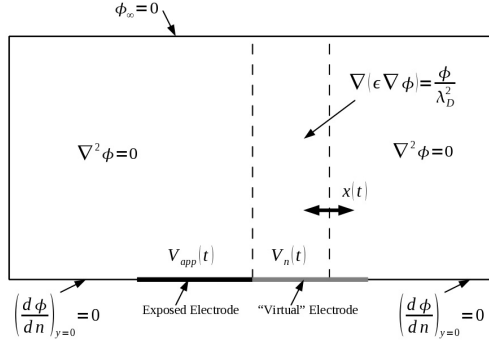
Before Equation 2.3 can be solved for the voltage potential, the relation between  $\phi$  and  $\rho$  needs to be established. The net charge density can be written as the difference between the ion density  $n_i$ , and the electron density  $n_e$ , multiplied by the elemental charge of an electron,  $e$ , namely

$$\rho = e(n_i - n_e). \quad (2.4)$$

The ion and electron densities can be related to the electric potential through the Boltzmann relation as

$$n_{i,e} = n_0 \exp[\mp(e\phi/kT_{i,e})], \quad (2.5)$$

where  $n_0$  is the background plasma density,  $k$  is the Boltzmann's constant, and  $T$  is the temperature of the particular species. Substituting Equation 2.5 into Equation 2.4 and

FIGURE 5. Computational domain with boundary conditions for  $\phi$ .

using a Taylor series approximation yields,

$$\rho = -\frac{\epsilon_0}{\lambda_D^2} \phi, \quad (2.6)$$

where  $\lambda_D$  is the Debye length given as

$$\frac{1}{\lambda_D^2} = \frac{e^2 n_0}{\epsilon_0} \left( \frac{1}{kT_i} + \frac{1}{kT_e} \right). \quad (2.7)$$

Since this is a non-thermal plasma, the species temperatures do not significantly change, meaning that  $\lambda_D$  can be assumed to be constant. For this work, a value of 0.17 mm, which is typical for plasmas of industrial interest (Roth 1995), was used.

Substituting Equation 2.6 into Equation 2.3 gives a Poisson equation in the electric potential,  $\phi$ , namely

$$\nabla \cdot (\epsilon_r \nabla \phi) = \frac{\phi}{\lambda_D^2}. \quad (2.8)$$

A final expression for the body force,  $\vec{f}_B$ , is found by substituting Equations 2.2 and 2.6 into Equation 2.1. The result is

$$\vec{f}_B = \frac{\epsilon_0}{\lambda_D^2} \phi \nabla \phi = -\frac{\epsilon_0}{\lambda_D^2} \phi \vec{E}. \quad (2.9)$$

The body force then involves the electric potential distribution that can be found from the solution of Equation 2.8.

This quasi-static formulation of the plasma actuator body force can be solved at small time steps of the AC period, assuming that the time steps are long compared to the charged particle recombination time scale,  $10^{-6}$  s. Note the typical AC period used in experiments is of the order of  $10^{-3}$  s.

Our approach to solving Equation 2.8 is to formulate it as a boundary value problem. Figure 5 shows the 2-D spatial domain over which it is solved. The experiments (Orlov 2006; Orlov *et al.* 2006) indicate that the plasma only forms over a portion of the dielectric material covering the lower electrode. It is in that region where Equation 2.8 applies. Outside of that region, the air is not ionized and the governing equation for the electric potential,  $\phi$ , is

$$\nabla \cdot (\epsilon_r \nabla \phi) = 0 \quad (2.10)$$

or  $\nabla^2 \phi = 0$ . The boundary between these two regions,  $x(t)$  changes in time as the plasma sweeps out over the dielectric material covering the encapsulated electrode.

The outer boundaries are taken to be far enough away from the electrodes as to

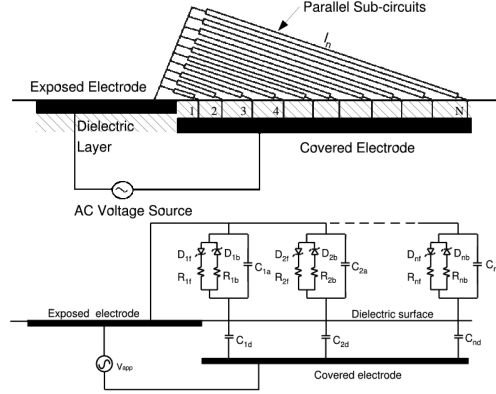


FIGURE 6. Schematic of parallel circuit configuration (top) and the circuit diagram for the sub-circuits (bottom).

approximate a boundary at “infinity” where the electric potential is zero, namely

$$\phi|_{outerboundary} = 0. \quad (2.11)$$

The boundary conditions for the electric potential on the electrodes are

$$\phi(t)|_{exposed-electrode} = \phi_0 \sin(\omega t) \quad (2.12)$$

and

$$\phi(t)|_{covered-electrode} = \phi_0 \sin(\omega t + \pi). \quad (2.13)$$

In order to complete the boundary value formulation, the electric potential boundary condition *on the surface of the dielectric material* is needed. This is the most important boundary condition because it is the one that models the charged particle dynamics that is evident from the time-resolved light emission experiments highlighted in Figure 3.

### 2.1. Lumped-element Circuit Model

The approach to obtain the electric potential on the dielectric surface comes from Orlov (2006); Orlov *et al.* (2006). It involves a lumped element circuit model that can simulate the space-time variation of the plasma for an AC-driven dielectric barrier discharge. This model takes into account the resistive and capacitive behavior of air as well as the capacitive properties of the dielectric material. A schematic of the circuit model is shown in Figure 6. It is a variation on the simple circuit model first suggested by Enloe *et al.* (2004a), who showed that a capacitive circuit analogy described the DBD actuator well. It consists of  $N$  parallel sub-circuits, in which the values of the circuit components depend on geometric parameters and physical constants. Each circuit consists of an air capacitor, a dielectric capacitor, and two air resistors with diodes that set the ionization threshold voltage. The diodes also serve to switch between the two resistors depending on the direction of the current. Two air resistors are needed because experiments have indicated that the electrons do not leave the surface of the dielectric as easily as they leave the uncovered metal electrode.

The schematic representation of an air circuit element is shown in the top part of Figure 7. Based on this, the value of the air capacitor of the  $n$ -th sub-circuit is given by

$$C_{na} = \frac{\epsilon_0 \epsilon_a A_n}{l_n}, \quad (2.14)$$

where  $\epsilon_a$  is the dielectric coefficient of the air,  $l_n$  is the distance over the surface of the



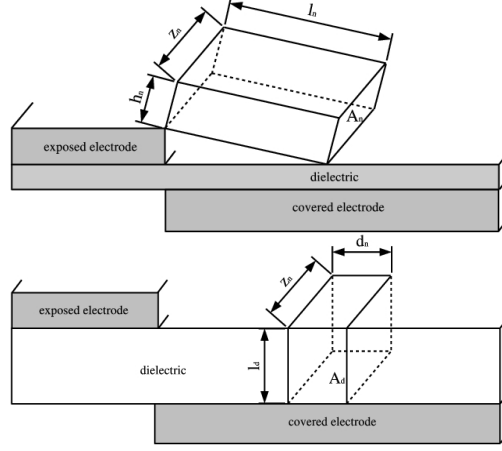


FIGURE 7. Schematic of air circuit element (top) and dielectric circuit element (bottom).

dielectric, and  $A_n$  is the cross-sectional area of the air capacitor (the product of the spanwise size of the actuator,  $z_n$ , and the height of the capacitive element,  $h_n$ ). The capacitive element height,  $h_n$ , is equivalent to the approximate height of the plasma which was estimated to be 1 mm.

The value of the air resistance of the  $n$ -th sub-circuit is given by

$$R_n = \frac{\rho_a l_n}{A_n}, \quad (2.15)$$

where  $\rho_a$  is the effective resistivity of air.

The schematic representation of a dielectric circuit element is shown in the bottom part of Figure 7. The value of the dielectric capacitor depends on the properties of the dielectric material. For the  $n$ -th sub-circuit, the dielectric capacitor is

$$C_{nd} = \frac{\epsilon_0 \epsilon_d A_d}{l_d}, \quad (2.16)$$

where  $\epsilon_d$  is the dielectric coefficient of the material,  $l_d$  is the thickness of the dielectric material, and  $A_d$  is equal to the product of the spanwise size of the actuator  $z_n$  and the width of the dielectric capacitive element,  $d_n$ .

By completing the circuit analysis for the  $n$ -th element, the equation for the time-varying voltage on the surface of the dielectric barrier at the  $n$ -th node is given as

$$\frac{dV_n(t)}{dt} = \left( \frac{C_{na}}{C_{na} + C_{nd}} \right) \frac{dV_{app}(t)}{dt} + k_n \frac{I_{np}}{C_{na} + C_{nd}}, \quad (2.17)$$

where  $I_{np}$  is the current through the  $n$ -th plasma resistor and  $V_{app}$  is the voltage applied to the exposed electrode. The zener diodes are modeled by the constant  $k_n$ . The zener diodes act to apply the threshold below which plasma will not form. If the electric field magnitude, given as

$$E_n = \frac{|V_{app} - V_n|}{l_n}, \quad (2.18)$$

is greater than some critical electric field,  $E_{crit}$ , needed for ionization (plasma formation), then  $k_n = 1$ . Otherwise,  $k_n = 0$ . The node where  $k_n$  switched from 1 to 0 defines the extent of the plasma ( $x(t)$  in Figure 5). The plasma current through the  $n$ -th plasma

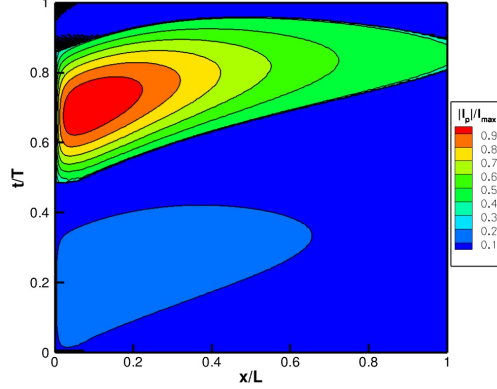


FIGURE 8. Space-time variation of rectified current obtained from lumped circuit model for SDBD plasma actuator corresponding to one period,  $T$ , of the input AC cycle.

resistor is given as,

$$I_{np}(t) = \frac{1}{R_n} [V_{app}(t) - V_n(t)], \quad (2.19)$$

where  $R_n = R_{nf}$  or  $R_{nb}$  depending on the direction of the current (forward,  $f$ , or backward,  $b$ ).

The method of solution involved combining Equations 2.17 and 2.19 to eliminate  $I_{pn}$  and formulate an initial value problem of the form

$$\frac{dV_n(t)}{dt} = f(t, V_n). \quad (2.20)$$

A 5th/6th order Runge-Kutta solver was used to solve Equation 2.20 for the voltage potential at each node at each new time step. It was assumed that the dielectric surface was initially uncharged, namely  $V_n = 0$  at  $t = 0$ . For all other time steps, the initial condition was the  $V_n$  values from the previous time step.

An example of the solution is shown through the space-time distribution of the rectified current  $|I_{np}(t)|$  that is presented in Figure 8. This shows contours of constant normalized current magnitude. The horizontal axis is the normalized location over the covered electrode,  $x/L$ . The vertical axis is time normalized by the AC period. Enloe *et al.* (2004a) had shown that the plasma light emission was proportional to the actuator current. A comparison between Figure 8 and the measured space-time plasma light emission in Figure 3 shows the same general features. These include two amplitude peaks during the AC cycle that originate from the edge of the exposed electrode ( $x/L = 0$ ), and a sweep-out over the covered electrode. Note that the simulation was performed at a higher input voltage which accounts for the increased extent of the plasma. However, Orlov (2006); Orlov *et al.* (2006) has previously shown that the current from the lumped circuit element model is able to reproduce the plasma extent and propagation velocity seen in the light emission experiments.

The circuit model was designed to provide the time-dependent boundary condition,  $V_n(t)$ , that exists on the surface of the dielectric in response to the driven AC voltage at the electrodes. This boundary condition was needed to solve the electrostatic Equations 2.8 and 2.10 to obtain the spatial distribution of the electric potential,  $\phi(x, y)$ , at small time increments in the actuator AC cycle. This was then used to determine the body force vector field according to Equation 2.9.

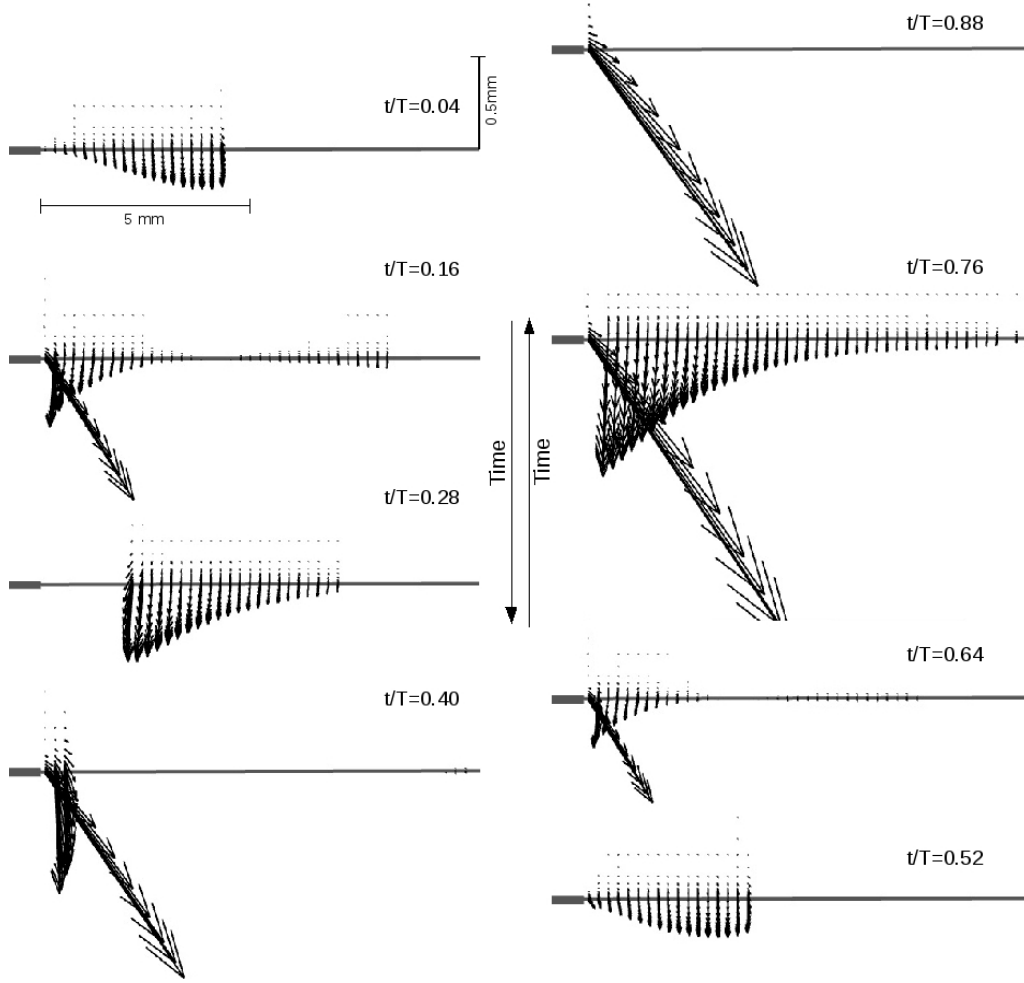


FIGURE 9. Time dependent body force vector field obtained from plasma actuator simulation.

## 2.2. Body Force Model Results

The solution of the model equations 2.17 and 2.19 respectively give the voltage on the surface of the dielectric,  $V_n(t)$ , and the current,  $I_{np}(t)$ , for each parallel circuit element.

A representative time dependent body force vector field during the AC cycle is shown in Figure 9 for a nominal input voltage amplitude of 5 kV at a frequency of 5 kHz. Each plot in the figure corresponds to a time increment of 12% of the AC period. The spatial scales are indicated in the plot at  $t/T = 0.04$ . Note that the wall-normal scale has been magnified in comparison to the horizontal scale. The thick horizontal lines represent the two electrodes in the staggered arrangement that was shown in the illustration in Figure 1. The thin horizontal line represents the surface of the dielectric. The magnitude scale of the body force vectors is the same in all of the plots (the largest magnitude during the AC cycle is approximately  $0.1 \text{ N/mm}^3$ ). Time is increasing from top to bottom in the left column of vector plots, and from the bottom to the top in the right column of plots.

The dynamic nature of the body force vector field within the AC cycle is clearly evident. At the initial time step,  $t/T = 0.04$ , the body force vectors are relatively small in magnitude and predominantly wall-directed. They cover approximately the first half

of the dielectric that is closest to the exposed electrode. In the next time increment,  $t/T = 0.16$ , larger magnitude body force vectors begin to form near the edge of the exposed electrode. These larger vectors have a horizontal component that is directed away from the exposed electrode. The vector field appears to convect away from the exposed electrode by the next time step,  $t/T = 0.28$ , and the predominant vector direction becomes wall-directed. This is followed by a sharp initiation of the body force at the next time step,  $t/T = 0.40$ , that includes larger magnitude vectors. This diminishes in the next time step at  $t/T = 0.52$  which is the approximate start of the next half of the AC cycle.

The process essentially repeats in the second half of the cycle,  $0.52 \leq t/T \leq 0.88$ , although the magnitudes of the body force vectors are noticeably larger than in the previous half-cycle. This reflects the differences between the two halves of the AC cycle that was evident in the time-resolved plasma illumination cycle that was shown in Figure 3, and replicated in the rectified current plot in Figure 8.

### 2.3. Body Force Validation

Our objective was to experimentally validate the time-resolved body force obtained from the model. Measuring the actuator body force on the AC time scale poses a bit of a challenge. Enloe *et al.* (2008) mounted a plasma actuator on a torsional pendulum. The actuator AC frequency was selected to couple with the natural frequency of the structure. Their approach was to subtract off the restoring force due to the elasticity of the structure to determine the actuator component. The difficulty in that approach was that it involved taking the difference between forces of comparable magnitude. In spite of this, they were able to determine that each half of the AC cycle produced a force that acted in the same direction but with different magnitudes.

The limitations of the Enloe *et al.* (2008) approach led us to seek another method to measure the time-resolved body force. It has been commonly observed that plasma actuators produce an acoustic “tone” that is correlated with the input AC frequency (Enloe *et al.* 2004a; Porter *et al.* 2006). Our approach was to relate the acoustics generated by the actuator to the time-resolved body force.

A schematic of the experimental setup is shown in Figure 10. The intention was to design the actuator to satisfy the conditions of a compact acoustic source. The AC input was a sinusoid with a frequency of 1 kHz. This resulted in an acoustic wavelength,  $\lambda$ , of 34.3 cm. The actuator electrodes were 7.6 cm long in the spanwise direction, which was approximately  $1/4\lambda$ . The actuator was placed in the center of a 3.7 m square ground plane, which then placed it approximately  $5\lambda$  from an edge.

The plasma actuator and ground plane were placed inside a 9.14 m long by 7.32 m wide by 3.66 m high anechoic room. The anechoic treatment consists of 56 cm thick fiberglass wedges that cover all four walls and ceiling and floor of the room. The room has a low-frequency cut-off of at least 150 Hz. Above the cut-off frequency, the wedges have a coefficient of energy absorption of 0.99.

Sound pressure measurements were taken along a 1.5 m circular arc from the actuator, in  $5^\circ$  increments. This corresponded to  $4.5\lambda$ . Sound pressure time series measured using a quarter-inch ACO model 7016 condenser microphone with an ACO model 4016 microphone pre-amplifier. The voltage time series proportional to the sound level fluctuations were sampled at 20 kHz (20 times the AC frequency). The AC time series to the plasma actuator was also simultaneously sampled to provide a phase reference.

Figure 11 shows the sound pressure auto-spectral density at an arc angle of  $60^\circ$ , as measured from the plane of the dielectric surface in the counter-clockwise direction. The actuator produced a large spectral peak at the AC frequency (1 kHz) as well

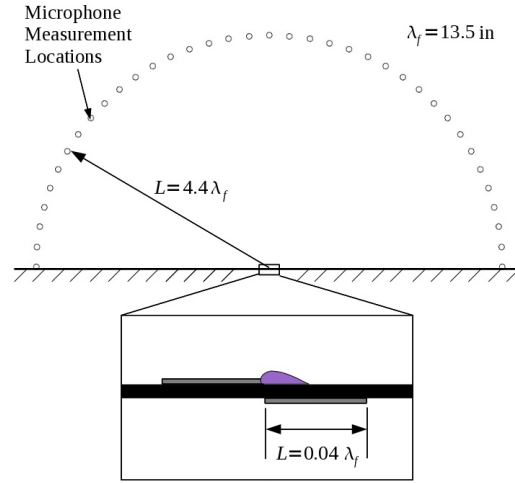


FIGURE 10. Schematic of acoustic measurement setup of time-dependent body force vectors produced by plasma actuator.

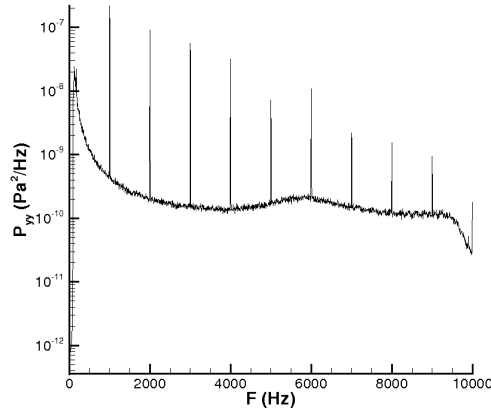


FIGURE 11. Sound pressure auto-spectral density that was measured at an arc angle of  $60^\circ$  from the plane of the dielectric surface of a plasma actuator with an AC frequency of 1 kHz.

as at higher harmonics. Considering only the sound pressure level at 1 kHz, Figure 12 documents the sound pressure level distribution around the measurement circular arc. The directivity pattern agrees well with that of an acoustic dipole oriented at a  $50^\circ$  angle.

The phase of the sound pressure time series at 1 kHz as a function of the angular position along the circular arc is shown in Figure 13. This indicates an approximate  $180^\circ$  phase shift at the angular position of  $140^\circ$ , which is where the sound pressure level amplitude was a minimum. This further supports the indication that the plasma actuator is behaving as an acoustic dipole.

### 2.3.1. Acoustic Analysis of Model

In order to compare the body force vectors from the plasma actuator model to the sound pressure measurements, the fluctuating forces need to be related to the fluctuating pressures in the far-field. This relation is derived by starting with the Helmholtz equation,

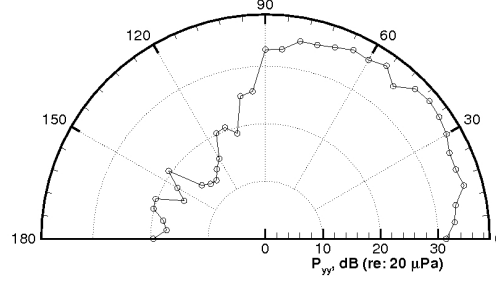


FIGURE 12. Sound pressure amplitude distribution at the AC frequency around a circular measurement arc from a plasma actuator.

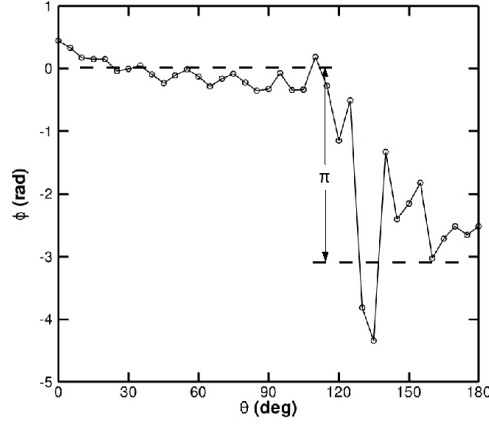


FIGURE 13. Phase of acoustic signal at the AC frequency as a function of the arc angle position from a plasma actuator.

$$\nabla^2 p + k^2 p = \nabla \cdot \mathbf{F}, \quad (2.21)$$

where  $p$  is the Fourier transform of the acoustic pressure and  $k$  is the acoustic wave number. Since the experiments indicate that the actuators have a behavior that is similar to that of an acoustic dipole, the acoustic source on the right-hand side of the equation is assumed to be of the form of a dipole, and  $\mathbf{F}$  is the equivalent body force density distribution. Equation 2.21 is valid for low Mach number systems without mono-pole or quadrapole type sources.

A Green's function approach can be used to solve the Helmholtz equation. The Green's function,  $G(\mathbf{r}, \mathbf{r}_0)$  is explicitly defined by the equation,

$$\nabla^2 G(\mathbf{r}, \mathbf{r}_0) + k^2 G(\mathbf{r}, \mathbf{r}_0) = -\delta(\mathbf{r} - \mathbf{r}_0) \quad (2.22)$$

and the appropriate boundary conditions for the system. In Equation 2.22,  $\mathbf{r}$  is the observer location (these are the measurement locations illustrated in Figure 10),  $\mathbf{r}_0$  is the source location, and  $\delta$  is the Kronecker delta function. The solution of Equation 2.21 is written as a convolution over the source region volume,  $V_0$ , of the Green's function,  $G(\mathbf{r}, \mathbf{r}_0)$ , and the distributed sources,  $\nabla \cdot \mathbf{F}$ , namely

$$p(\mathbf{r}) = \iiint_V [-\nabla_0 \cdot \mathbf{F}] G(\mathbf{r}, \mathbf{r}_0) dV_0, \quad (2.23)$$

where the operator subscript of the operator  $\nabla_0$  denotes operation of the source region. A detailed derivation of Equation 2.23 can be found in Morse & Ingard (1968), among others. Since only the far-field pressure is of interest for this application, integration by parts can be used to rewrite Equation 2.23 as

$$p(\mathbf{r}) = \iiint_V \mathbf{F} \cdot \nabla_0 G(\mathbf{r}, \mathbf{r}_0) dV_0. \quad (2.24)$$

In this analysis, the free-space Green's function,

$$G_{fs} = \frac{e^{ik|\mathbf{r}-\mathbf{r}_0|}}{4\pi|\mathbf{r}-\mathbf{r}_0|}, \quad (2.25)$$

was used for  $G(\mathbf{r}, \mathbf{r}_0)$ . The gradient of Equation 2.25 in the far-field is given by

$$\nabla_0 G_{fs}(\mathbf{r}, \mathbf{r}_0) = -[ik \cos(\theta)] G_{fs}(\mathbf{r}, \mathbf{r}_0), \quad (2.26)$$

where  $\theta$  is the angle between the axis of the dipole forces and the vector between the source and receiver,  $\mathbf{r} - \mathbf{r}_0$ . Substituting Equation 2.26 into Equation 2.24 yields,

$$p(\mathbf{r}) = - \iiint_V \mathbf{F} [ik \cos(\theta)] G_{fs}(\mathbf{r}, \mathbf{r}_0) dV_0. \quad (2.27)$$

Further simplifications can be made if  $|\mathbf{r} - \mathbf{r}_0|$  can be approximated as  $|\mathbf{r}|$ . This is a reasonable assumption since  $|\mathbf{r}| \gg |\mathbf{r}_0|$ . Using this approximation and knowing that  $\mathbf{r}_0$  does not significantly affect  $G_{fs}$ ,  $G_{fs}$  can be removed from the integral in Equation 2.27. Furthermore, assuming  $\mathbf{F}$  represents a compact point source, this integral becomes trivial because  $\mathbf{F}$  is assumed to be constant over the source volume. This assumption of compactness can be written as  $k|\mathbf{r}_0| \ll 1$ , since the coordinate system being used is centered about the source region. Evaluating the integral in Equation 2.27 yields

$$p(\mathbf{r}) = -ik|\mathbf{F}^*|G(\mathbf{r}, \mathbf{r}_0) \cos(\theta), \quad (2.28)$$

where  $\mathbf{F}^*$  is the body force vector (as opposed to body force density). The auto-spectrum of the acoustic pressure can be found by multiplying the results of Equation 2.28 by its complex conjugate. This yields

$$\Phi_{pp}(\omega) = \overline{p^2}(\mathbf{r}) = k^2 |G_{fs}^2| \cos^2(\theta) \Phi_{ff}(\omega), \quad (2.29)$$

where  $\Phi_{ff}(\omega)$  is the auto-spectrum of the body force. The wave number can also be taken to be,  $k = \omega/c_0$ , and substituting this relation and Equation 2.25 into Equation 2.29 gives

$$\Phi_{pp}(\omega) = \frac{\omega^2}{16\pi^2 c_0^2 \mathbf{r}^2} \cos^2(\theta) \Phi_{ff}(\omega). \quad (2.30)$$

Equation 2.30 can be used to relate the auto-spectrum of the body force vectors generated by the numerical plasma model,  $\Phi_{ff}(\omega)$ , to the auto-spectrum of the sound pressure level,  $\Phi_{pp}(\omega)$ , which can be compared to the sound pressure level measurements.

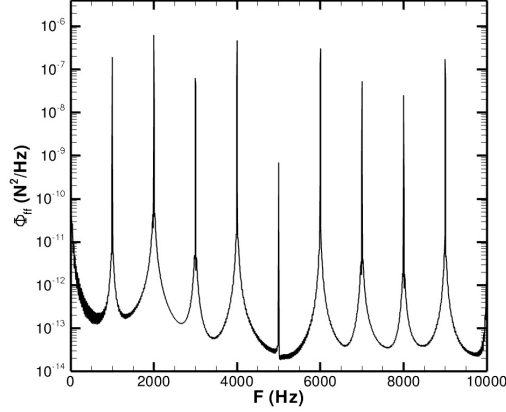


FIGURE 14. Auto-spectra of the largest magnitude body force vector from the SDBD plasma actuator model with an AC frequency of 1 kHz.

The simulation of the time dependent body force vector field was used to generate a contiguous time series that was long enough to obtain its auto-spectra. The time series consisted of  $10^7$  points that were “sampled” at 500 kHz. The assumption of a compact source means that the vector field must be represented by a “single” vector. We investigated this by using the largest magnitude vector at each time-step, as well as the six largest magnitude vectors at each time step. The largest magnitude vectors were always closely spaced and near the edge of the exposed electrode. An example of the spectrum of the body force time series from the plasma actuator model is shown in Figure 14. The spectral peak at the AC input frequency (1 kHz) was numerically integrated using the trapezoidal method to obtain the auto-spectral density of the body force at 1 kHz,  $\Phi_{ff}(2\pi \text{ krad/s})$ , which was substituted into Equation 2.30. The orientation of the dipole force was found by individually calculating the auto-spectrum of both components (streamwise,  $x$ , and wall-normal,  $y$ ) of the body force vectors at 1 kHz, and using the arc-tangent of the ratio between these values to find the resultant angle, namely

$$\theta_f = \arctan \left( \frac{\Phi_{F_y}(2\pi \text{ krad/s})}{\Phi_{F_x}(2\pi \text{ krad/s})} \right). \quad (2.31)$$

The angle,  $\theta$ , in Equation 2.30 is the difference between the microphone position angle,  $\theta_m$ , and the dipole orientation angle,  $\theta_f$ , that is  $\theta = \theta_m - \theta_f$ . The speed of sound,  $c_0$  is taken to be 343 m/s (assuming a temperature of 20°C)(Pierce 1989). The radius,  $r$ , is 1.52 m (5 ft) and  $\omega = 2\pi \text{ krad/sec}$ . The resultant directivity pattern is plotted in Figure 15 versus the experimentally measured pattern. In this case the six largest magnitude body force vectors were used.

The acoustic directivity pattern that was generated from the time-dependent plasma actuator model has many of the features observed in the experiment. This includes the dual-lobed shape and the 50° maximum directivity angle, where the sound pressure level is a maximum. When the six largest vectors were considered, the agreement with the experiment between the angles of 0° to 90° was within 1.5 dB (4.2%).

The dipole distribution does not capture all of the measured directivity pattern features beyond 90°. In particular it over-predicts the magnitude of the smaller lobe. Some of the discrepancy in this range of angles could be due to experimental uncertainty. It was noted that the phase coherence between the measured sound pressure level and the actuator input was the lowest in this range of measurements angles. The discrepancies could also



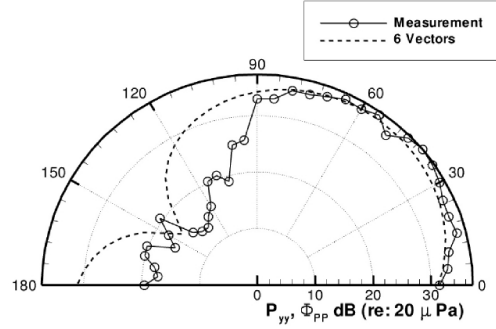


FIGURE 15. Directivity pattern produced by time-dependent plasma actuator model based on free-space Green’s function using the six largest magnitude body force vectors.

be caused by the fact that true dipole forcing would have a push-pull (momentum added in the stream-wise during one half cycle and momentum added in the negative stream-wise direction in the other half cycle) behavior during the two half cycles. Our DBD plasma actuator model predicts a PUSH-push behavior (where “PUSH” corresponds to a “large” momentum addition in the positive  $x$  direction during one half cycle and “push” corresponds to a “smaller” addition of momentum but still in the same positive  $x$  direction during the second half cycle. This is consistent with the plasma actuator driven torsional pendulum experiment of Enloe *et al.* (2008). This is not accounted for in the acoustic analogy used in this analysis, and could be a factor in the poorer comparison with the experimental directivity pattern beyond the  $90^\circ$  measurement angles where the effect of the “back” stroke would be most strongly felt. However, in general, the time-dependent body force that emerges from our simulation is reasonably validated by the acoustic measurements.

### 2.3.2. Static Body Force Scaling

As pointed out in Section 1, numerous experiments have indicated that the static thrust produced by a SDBD plasma actuator in still air, scales as  $V_{AC}^{3.5}$ . An example from Iqbal *et al.* (2007) was shown on Figure 4. Iqbal *et al.* (2007) among others (Enloe *et al.* 2004b; Forte *et al.* 2006; Post 2001, 2004) further verified the consistency between the reaction force and the fluid momentum in the air stream generated by the actuator. As a result, the body force also must scale as  $V_{AC}^{3.5}$ .

The thrust measured in experiments is a time average over many AC cycles of the reaction force produced by plasma actuator. In order to compare the time-resolved body force vector field from the model with the experimental measurements, we computed an average body force given by the spatial average of the RMS of the time-varying body force magnitudes. This was performed on the plasma actuator simulation for a range of AC voltages. The result is presented in Figure 16. The results from the model are plotted on log-log axes to highlight the power-law scaling of the body force (note that the forces are scaled with reference to the maximum force of  $1.2 \text{ mN/mm}^3$ , but this does not have any effect on the observed power-law scaling). The straight line through the four force values at the lower AC voltages is a best-fit of  $F = AV_{p-p}^m$ . This fit gave  $m = 3.49$  which is very close to the experimentally observed value of 3.5. The line through the force values at the two highest voltages is a separate power-law fit. This gave a best-fit exponent value of 2.67. This compares to 2.3 in Figure 4 that was given by Thomas *et al.* (2010). The deviation from the  $V^{3.5}$  scaling is thought to be a result of having a

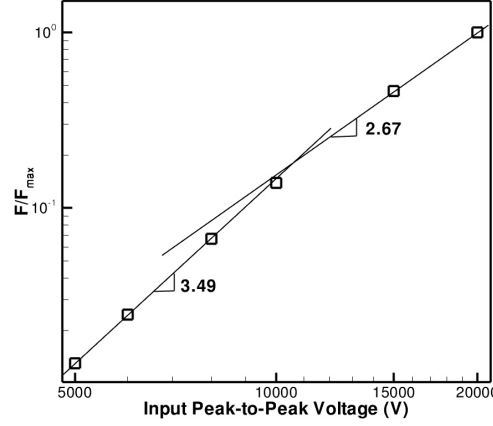


FIGURE 16. Body force versus applied AC voltage from SDBD plasma actuator model.

covered electrode that is too small and thereby causing a charge build-up on the dielectric that reduces the electric field and body force. Based on experiments, there is no observed universality to this exponent, which likely depends on the specific electrode configuration. The important validation result from our plasma actuator model is that it predicts this decrease in the body force at higher voltages.

### 3. Flow Simulation Results

Two experiments were chosen in which to compare flow simulations utilizing the plasma actuator model. These were an impulsively started plasma actuator on a wall in quiescent air by Post (2004) and high Reynolds number flow around a circular cylinder with plasma actuators that was designed to suppress the Karman vortex street by Thomas *et al.* (2008).

#### 3.1. Impulsively Started Flow

The impulsively started plasma actuator experiment consisted of a SDBD plasma actuator that was located on one wall of a large-volume rectangular container. The design of the actuator was the same as that shown in Figure 1. The air in the container was seeded with particles. The flow field induced by operating the plasma actuator was measured with a Particle Image Velocimeter (PIV). The laser sheet for the PIV system formed a 2-D plane in the wall-normal and induced mean flow directions. It was aligned with the spanwise centerline of the plasma actuator. The plasma actuator was cycled on and off with a 50% duty cycle at a low (1 Hz) frequency. The PIV laser was triggered following an adjustable time delay from when the plasma actuator first cycled on. Multiple PIV images were then sampled at a fixed time delay to obtain the phase-averaged spatial velocity field at a specified time increment. This was repeated for different time delays. The phase-averaged velocity field at four time increments from Post(2004) is shown in the left part of Figure 17.

The simulation of the Post experiment was performed in a domain that was comparable to the 0.25 m by 0.25 m dimensions of the physical enclosure. This corresponded to approximately 10 times the largest dimension of the plasma actuator. The computational grid consisted of 400 points in the induced mean flow direction,  $x$ , and 180 points in the wall-normal,  $y$  direction. In the  $x$  direction, the grid was clustered near the plasma

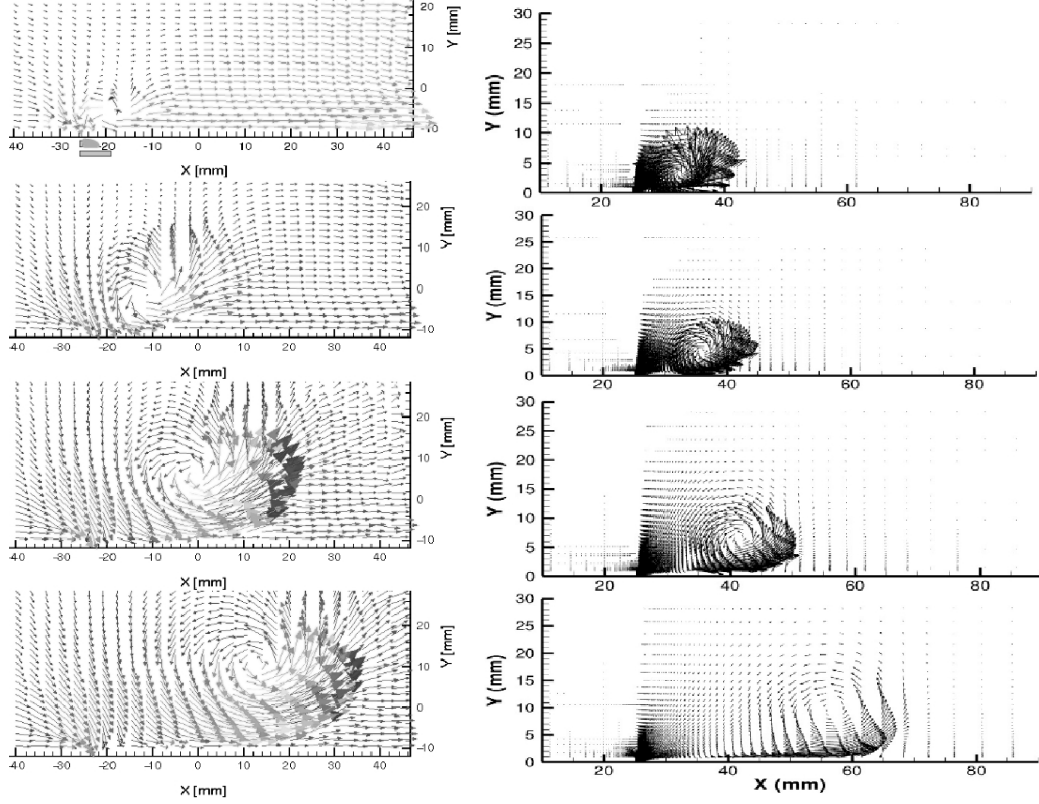


FIGURE 17. Velocity vector field at different time delays following an impulsively started plasma actuator. Post (2004) experiment shown on the left. Simulation using plasma actuator model on the right.

actuator to improve the spatial resolution in that region. In the  $y$  direction, the grid was clustered near the wall.

The governing equations were the 2-D, unsteady, incompressible, Reynolds-averaged Navier-Stokes (RANS) equations. The RANS equations consisted of the conservative equations for mass and momentum. The conservative momentum equation is given by

$$\frac{\partial}{\partial t}(\rho \vec{v}) + \nabla \cdot (\rho \vec{v} \vec{v}) = -\nabla p + \nabla \cdot (\bar{\tau}) + \rho \vec{g} + \vec{f}_b, \quad (3.1)$$

and includes the external body force term,  $\vec{f}_b$ . The body force vector field for the plasma actuator comes from the plasma actuator simulation described in the Section 2.2.

Because the flow was incompressible, the air density was found through the ideal gas relation. The turbulence model used in the formulation was the  $v^2 - f$  model developed by Durbin (1995).

No-slip and no-penetration boundary conditions were applied on all surfaces. The initial free-stream velocity in the enclosure was zero. Because the flow induced by the actuator was confined to the enclosure, some mean flow recirculation was generated. This however also occurred in the Post experiment, and was judged to have a minimal effect on the local flow field near the plasma actuator.

A second order implicit discretization scheme was used for both space and time. An algorithm (Mertz 2010) was used for the pressure-velocity coupling. This enforced mass

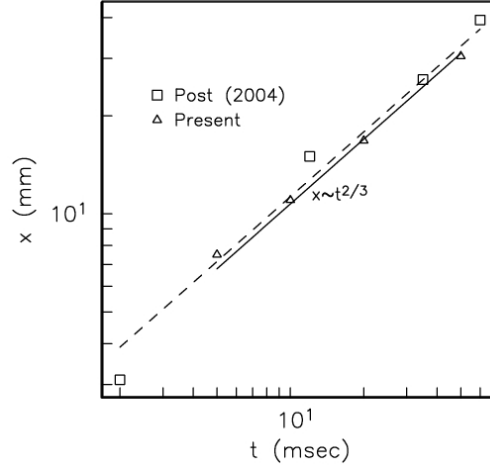


FIGURE 18. Streamwise ( $x$ ) position versus time of the vortex produced by the impulsively started plasma actuator.

conservation and calculated the pressure field using a relationship between velocity and pressure corrections.

The simulation of the impulsively started plasma actuator is shown in the right part of Figure 17 (for reference, the largest vectors have a magnitude on the order of 5 m/s). Velocity vectors for four different time delays of 5, 10, 20 and 50 ms are shown. The body force vector field came from a simulation that was based on a thin Kapton dielectric layer and a peak-to-peak AC voltage of 5 kV that were comparable to the Post (2004) experiment.

Both the experimental and simulation velocity vector fields indicate that the impulsively started plasma actuator produces a “starting vortex” with circulation in the counter-clockwise direction. As time progresses the vortex convects away from the plasma actuator (to the right).

In order to make a quantitative comparison between the experiment and simulation, the spatial trajectory of the starting vortex at each time increment shown in Figure 17 was measured. The streamwise,  $x$ , location of the vortex as a function of time is shown in Figure 18. This is based on an estimate of the center of the vortex. Log-log axes were used in plotting the streamwise position with time because theoretical analysis by Saffman (1978), that was demonstrated in the experiments by Auerback (1987), indicated that the streamwise location of the vortex increase with time to the two-thirds power, or  $x \propto t^{2/3}$ . Therefore the streamwise position of the starting vortex with time was expected to fall on a straight line with a  $2/3$  slope in the log-log representation.

Figure 18 shows excellent agreement between the Post (2004) experiment and present simulation of the  $x$  trajectory of the vortex produced by impulsively starting the plasma actuator. In addition it shows the  $t^{2/3}$  proportionality that was predicted by Saffman (1978). This therefore provides one of the simple but important flow validations of the plasma actuator simulations. The second flow validation applies to the flow around a circular cylinder with plasma actuators.

### 3.2. Cylinder Unsteady Wake Suppression

The simulation of the flow around a circular cylinder with plasma actuators was designed to match the experiment by Thomas *et al.* (2008). The circular cylinder in the experiment was made of quartz glass. It had an outer diameter,  $D$ , of 100 mm. The cylinder was

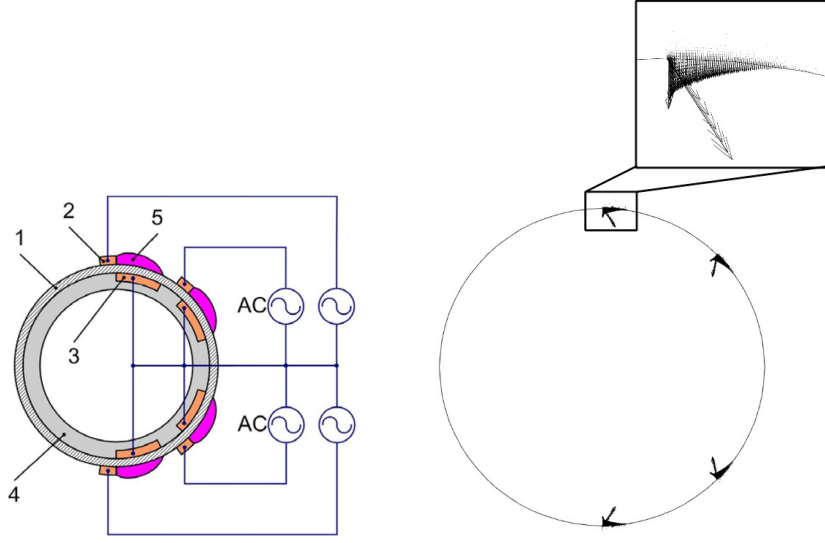


FIGURE 19. Schematic of circular cylinder with four SDBD plasma actuators from Thomas *et al.* (2008) (left) and time-averaged body force vector distribution computed from present SDBD plasma actuator model.

hollow with a wall thickness of 2.5 mm. The glass wall was the dielectric layer between the electrodes of the plasma actuators. Its dielectric coefficient is  $\epsilon_d = 3.7$ . Four plasma actuators were placed around the cylinder corresponding at angular positions of  $\pm 90^\circ$  and  $\pm 135^\circ$  with respect to the flow direction. A schematic drawing of the cylinder with plasma actuators is shown in the left part of Figure 19. The time-averaged body force distribution for the four plasma actuators based on the present SDBD model is shown on the right side of Figure 19. A sinusoidal waveform with an AC frequency of 10 kHz and an peak-to-peak amplitude of 11.5 kV was used in the flow simulation. This is comparable to the experiment. The experiment and simulation were performed at a  $Re_D = 33,000$  (based on the cylinder diameter and a free stream velocity  $U_\infty = 4$  m/s).

The formulation for the flow simulation was similar to that of the previous impulsively started plasma actuator flow simulation. In this case a 2-D triangular mesh of grid points with approximately 172,000 nodes was used. All of the far-field boundaries were at least 15 cylinder diameters from the cylinder. Near the cylinder, a rectangular boundary layer grid was used. The grid points were clustered near the actuator locations in order to resolve the body force vector field that was generated by the SDBD plasma actuator model. The entire grid and a magnified view of the grid near the cylinder are shown in Figure 20. The flow simulation used a  $k-\omega$  turbulence model(Menter 1994).

An example of the results from the simulation is presented in Figure 21. This shows particle streak lines that are marking the flow around the cylinder with the plasma actuators off and on. Included at the top of the figure are time-averaged flow visualization images from Thomas *et al.* (2008) for the same conditions as the simulations. Both show a similar suppression of the Karman vortex street that results from the plasma actuators.

A more quantitative comparison can be made between the simulation and experiments by examining the mean velocity profiles in the near wake region of the cylinder. Figure 22 shows spanwise profiles of the the normalized mean streamwise velocity component,  $U/U_\infty$ , at three streamwise locations of  $x/D = 2, 4$ , and 8. The symbols correspond to the experimental results. The curves correspond to the simulation results. The square

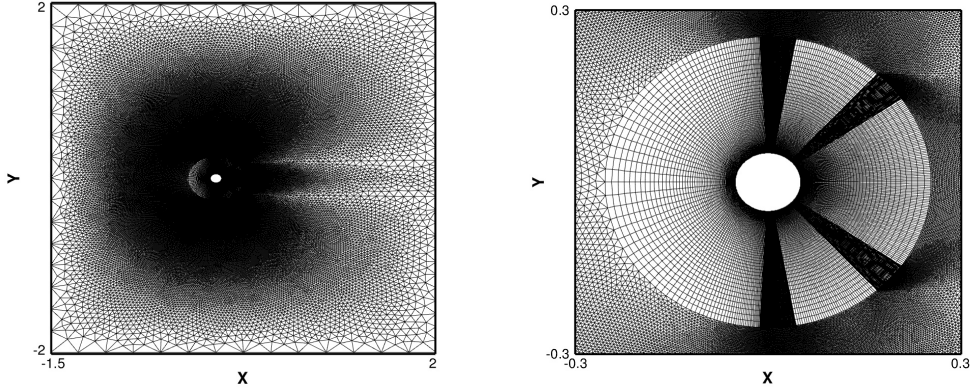


FIGURE 20. Computational mesh used for circular cylinder flow simulations with plasma actuators.

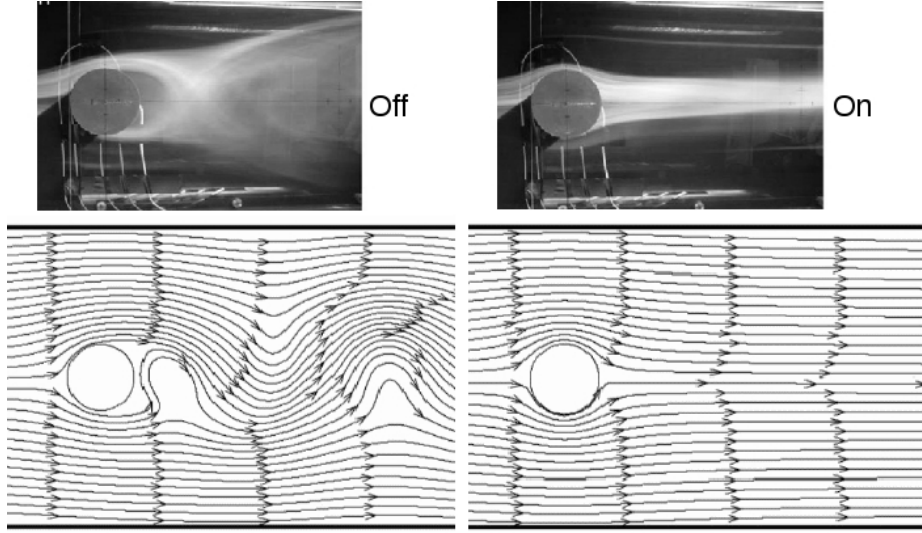


FIGURE 21. Particle streak lines from the simulation of the flow around a 2-D circular cylinder with plasma actuators off (left) and on (right), and a comparison to time-averaged flow visualization images (top) for the same conditions from Thomas *et al.* (2008).

symbols and the solid curve are with the plasma actuator off. The triangle symbols and the dashed curve correspond to the plasma actuators operating. Both the experiment and flow simulation show a near elimination of the wake deficit at the downstream locations that confirms the qualitative results from the flow visualization records. The simulation over-estimates the wake deficit in the baseline (actuator off) flow at the most upstream location, but agrees well with the wake profiles at all the locations with the plasma actuator operating. This good agreement between the simulation and experiment further validates the SDBD plasma actuator modeling approach.

#### 4. Conclusions

A semi-empirical model for single dielectric barrier discharge (SDBD) plasma actuators was presented. The model simulates the time-resolved spatial body force vector field. It was validated against an acoustic experiment in which the plasma actuator was designed

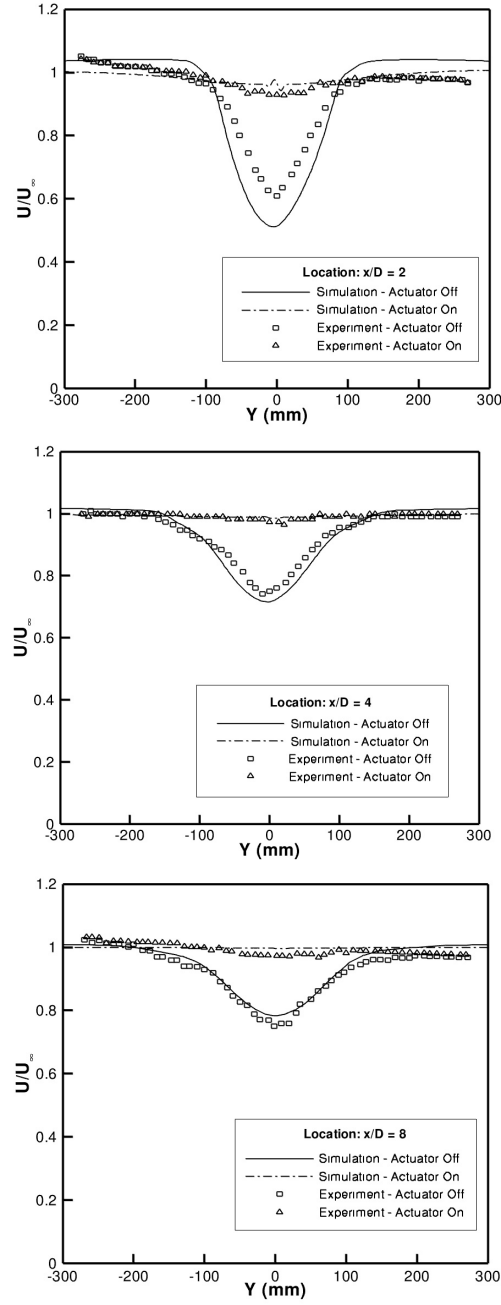


FIGURE 22. Comparison of streamwise component mean velocity profiles in the near wake of a circular cylinder from experiments (Thomas *et al.* 2008) and simulations using present plasma actuator model.

to satisfy the conditions of a compact acoustic source. Spectra of the model body force time series were used with a free-space dipole Green's function to obtain the acoustic spectral amplitude distribution around a constant radius arc encircling the upper half plane of the actuator. Excellent agreement was found between the simulated and experi-

mental acoustic distributions, in both directivity and amplitude. The results verified that the plasma actuator acts as an acoustic dipole.

The model was further validated by demonstrating that the time-average body force magnitude scaled with voltage to the 3.5 power as observed in experiments. In addition, the model simulated the asymptote in the body force magnitude that has been observed in experiments to occur at larger voltages when the area of the encapsulated electrode was too small.

Two flow simulations were used to validate the SDBD plasma actuator model. These involved an impulsively started plasma actuator in still air, and the flow around a circular cylinder in which plasma actuators were used to suppress the Karman vortex street. In both cases, the simulations agreed well with the experiments.

## REFERENCES

- AUERBACK, D. 1987 Experiments on the trajectory and circulation of the starting vortex. *J. Fluid Mech.* **183**, 185–198.
- BENGADRI, R., RABEHI, A., MASSINES, F. & SEGUR, P. August, 23–26, 1994, pp. 228–229 Numerical modelling of atmospheric pressure low-frequency glow discharge between insulated electrodes. In *Proceedings of the XIIth ESCAMPIG, Netherlands*.
- BOEUF, J. P., LAGMICH, Y., UNFER, T., CALLEGARI, T. & PITCHFORD, L. 2007 Electrohydrodynamic force in dielectric barrier discharge plasma actuators. *J. Phys. D.: Appl. Phys.* **40**, 652–662.
- CORKE, T., POST, M. & ORLOV, D. 2009 Single dielectric barrier discharge plasma enhanced aerodynamics: Physics, modeling and applications. *Exp. Fluids* **46**, 1–26.
- CORKE, T. C., POST, M. L. & ORLOV, D. M. 2007 Sdbd plasma enhanced aerodynamics: concepts, optimization and applications. *Prog. Aerospace Sci.* **43**, 193–217.
- DAVIDSON, G. & O’NEIL, R. 1964 Optical radiation from nitrogen and air at high pressure excited by energetic electrons. *J. Chem. Phys.* **41**, 3946–3949.
- DURBIN, P. A. 1995 Separated flow computations with the  $k$ - $\epsilon$ - $v^2$  model. *AIAA Journal* **33** (4), 659–664.
- ELIASSON, B. & KOGELSCHATZ, U. 1991 *IEEE Trans. Plasma Sci.* **19**, 309.
- ENLOE, C., MCHARG, M. & MCCLAUGHLIN, T. 2008 Time-correlated force production measurements of the dielectric barrier discharge plasma aerodynamic actuator. *J. App. Phys.* **103**.
- ENLOE, L., MCCLAUGHLIN, T., VANDYKEN, KACHNER, JUMPER, E. & CORKE, T. 2004a Mechanisms and responses of a single-dielectric barrier plasma actuator: Plasma morphology. *AIAA* **42**, 589–594.
- ENLOE, L., MCCLAUGHLIN, T., VANDYKEN, KACHNER, JUMPER, E., CORKE, T., POST, M. & HADDAD, O. 2004b Mechanisms and responses of a single-dielectric barrier plasma actuator: Geometric effects. *AIAA* **42**, 595–604.
- FALKENSTEIN, Z. & COOGAN, J. 1997 Microdischarge behaviour in the silent discharge of nitrogen-oxygen and water-air mixtures. *J. Phys. D: App. Phys.* **30**, 817–825.
- FORTE, M., JOLIBOIS, J., MOREAU, E., TOUCHARD, G. & CAZALENS, M. 2006 Optimization of a Dielectric Barrier Discharge Actuator by Stationary and Non-stationary Measurements of the Induced Flow Velocity - Application to Airflow Control. AIAA Paper 2006-2863.
- GIBALOV, V. & PIETSCH, G. 2000 The development of dielectric barrier discharges in gas gaps and surfaces. *J. Phys. D: Applied Phys.* **33**, 2618.
- IQBAL, M., CORKE, T. & THOMAS, F. 2007 Parametric optimization of single dielectric barrier discharge (sdbd) plasma actuators. *submitted AIAA J.*
- KOGELSCHATZ, U. 1997 In *Proc. Int. Conf. Phenomena Ionized Gases, ICPIG XXIII, Toulouse, FR*.
- MASSINES, FRANCOISE, RABEHI, AHMED, DECOMPS, PHILIPPE, BEN GADRI, RAMI, SEGUR, PIERRE & MAYOUX, CHRISTIAN 1998 Experimental and theoretical study of a glow discharge at atmospheric pressure controlled by dielectric barrier. *Journal of Applied Physics* **83**.



- MENTER, F. R. 1994 Two-equation eddy-viscosity turbulence models for engineering applications. *AIAA Journal* **32** (8), 1598–1605.
- MERTZ, B. E. 2010 Refinement, validation and implementation of lumped circuit element model for single dielectric barrier discharge plasma actuators. PhD thesis, University of Notre Dame.
- MORSE, P. M. & INGARD, K. U. 1968 *Theoretical Acoustics*. Princeton University Press.
- ORLOV, DMITRIY & CORKE, THOMAS 2005 Numerical Simulation of Aerodynamic Plasma Actuator Effects. AIAA Paper 2005-1083.
- ORLOV, DMITRIY, CORKE, THOMAS & HADDAD, OSAMAH 2003 DNS modeling of plasma array flow actuators. In *Bulletin of the American Physical Society Division of Fluid Dynamics*, , vol. 48.
- ORLOV, DMITRIY, CORKE, THOMAS & PATEL, MEHUL 2006 Electric Circuit Model for Aerodynamic Plasma Actuator. AIAA Paper 2006-1206.
- ORLOV, D., FONT, G. & EDELSTEIN, D. 2008 Characterization of discharge modes of plasma actuators. *AIAA J.* **46**, 3142–3148.
- ORLOV, DMITRI M. 2006 Modelling and simulation of single dielectric barrier discharge plasma actuators. PhD thesis, University of Notre Dame.
- PIERCE, A. D. 1989 *Acoustics: An Introduction to Its Physical Principles and Applications*. Acoustical Society of America.
- PORTER, C.O, BAUGHN, J.W., MCLAUGHLIN, T.E., ENLOE, C.L. & FONT, G.I. 2006 Temporal Force Measurements on an Aerodynamic Plasma Actuator. AIAA Paper 2006-104.
- POST, M. & CORKE, T. 2005 Overview of plasma flow control: Concepts, optimization, and application. AIAA Paper 2005-0563.
- POST, MARTIQUA L. 2001 Phased plasma actuators for unsteady flow control. Master's thesis, M.S. in Aerospace and Mechanical Engineering, University of Notre Dame.
- POST, MARTIQUA L. 2004 Plasma actuators for separation control on stationary and unstationary airfoils. PhD thesis, University of Notre Dame.
- RABEHI, A., BENGADRI, R., SEGUR, P., MASSINES, F. & DECOMPS, PH. October, 23-26, 1994, pp. 840-845 Numerical modelling of high pressure glow discharges controlled by dielectric barrier. In *Proceedings of the Conference on Electrical Insulation and Dielectric Phenomena*, Arlington, TX.
- ROTH, J.R. 1995 *Industrial plasma engineering*. Institute of Physics Publishing.
- SAFFMAN, P. G. 1978 The number of waves on unstable vortex rings. *J. Fluid Mech.* **84**, 625–639.
- SINGH, K. & ROY, S. 2008 Force approximation for a plasma actuator operating in atmospheric air. *J. App. Phys.* **103**, 013305.
- THOMAS, F., CORKE, T., IQBAL, M., KOZLOV, A. & SHATZMAN, D. 2010 Optimization of sdbd plasma actuators for active aerodynamic flow control. *AIAA J.* **47**, 9, 2169–2177.
- THOMAS, F., KOZLOV, A. & CORKE, T. 2008 Plasma actuators for bluff body flow control. *AIAA J.* **46**, 8.
- VIDMAR, R. & STALTER, K. 2003 Air chemistry and power to generate and sustain plasma: plasma lifetime calculations. , vol. AIAA 2003-1189.
- VOIKOV, V., CORKE, T. & HADDAD, O. 2004 Numerical simulation of flow control over airfoils using plasma actuators. In *Bulletin of the American Physical Society Division of Fluid Dynamics*, , vol. 49.